RSC Advances

PAPER

View Article Online
View Journal | View Issue

Cite this: *RSC Adv.*, 2016, **6**, 69016

Synthesis and electrochemical performance of Co_2TiO_4 and its core–shell structure of Co_2TiO_4@C as negative electrodes for Li-ion batteries

S. Yuvaraj,[a] R. Hari Vignesh,[b] L. Vasylechko,[c] Y. S. Lee[b] and R. Kalai Selvan*[a]

Received 1st May 2016
Accepted 26th June 2016

DOI: 10.1039/c6ra11251j

www.rsc.org/advances

Spinel Co_2TiO_4 is synthesised using a polymeric precursor method and used as an efficient negative electrode for Li-ion batteries. Precise full-profile Rietveld refinement proves the formation of a single-phase cubic spinel structure with a lattice parameter of $a = 8.4190(9)$ Å, which corresponds to the sample composition of $Co_{2.05}Ti_{0.95}O_4$. Subsequently, a carbon coating around Co_2TiO_4 is achieved through a simple hydrothermal method. TGA analysis implies that Co_2TiO_4@C consists of 17 wt% carbon, and the presence of D and G bands was confirmed through Raman analysis. Transmission electron microscopy (TEM) is employed to probe the morphological features, as well as to confirm the carbon coating on Co_2TiO_4. It shows non uniform shape particles with sizes in the range of 400–750 nm and that the thickness of the carbon coating is 10 nm. The superior electrochemical performance of Co_2TiO_4@C is confirmed by a higher initial discharge–charge capacity (1283/418 mA h g^{-1}), high diffusion coefficient (1.76×10^{-10} cm^2 $s^{-1/2}$) and lower R_{ct} (after 50 cycles). This is attributed to the increased electrical conductivity and the creation of new active sites due to the synergistic effect of the carbon matrix on Co_2TiO_4, thereby making it a promising candidate for lithium ion battery applications.

1. Introduction

Nowadays, research work is moving to the next paradigm by modifying either anode or cathode materials to achieve higher energy and power densities of lithium ion batteries.[1–3] Currently, graphite or $Li_4Ti_5O_{12}$ are used as anode materials while lithium based layered ($LiCoO_2$), olivine ($LiFePO_4$) and spinel ($LiMn_2O_4$) structured materials act as cathodes.[4–6] Graphite has several features including a high capacity (372 mA h g^{-1}) and flat working potential (0.2 V *vs.* Li^+/Li). But several demerits like the formation and growth of lithium dendrites at lower potentials cause safety issues, while a lower diffusion coefficient leads to poor rate capability.[7] On the other hand, $Li_4Ti_5O_{12}$ is considered as one of the alternative sources to graphite anodes, which operates at a 1.5 V (*vs.* Li^+/Li) working potential. This restricts electrolyte decomposition and formation of lithium dendrites, thereby giving further assurances such as safety along with zero strain during Li^+ intercalation/de-intercalation, leading to good cycling stability and high rate capability of the material.[8] However, high working potentials and low theoretical capacities are the main issues for enhancing the energy density of Li-ion batteries. Therefore, the commercially introduced graphite and $Li_4Ti_5O_{12}$ should be replaced by alternative anode materials which are safe and have high energy and power densities for application in electric vehicles.

In this perspective, much research work has been emphasized to find new titanium based anode materials. Recently, Lin *et al.* studied $TiNb_6O_{17}$ and $Ti_2Nb_{10}O_{29}$ as novel anode materials for Li ion batteries, which have a discharge capacity of 178 mA h g^{-1} and 90 mA h g^{-1} after 100 cycles at 5C rate.[9] Goodenough's group have investigated $TiNb_2O_7$ as a new anode material with a high voltage of 1.6 V *vs.* Li^+/Li. It delivers a large reversible capacity of 285 mA h g^{-1} at 0.2C over 30 cycles with 98% capacity retention without any SEI layer formation.[10] Ternary titanium based complexes such $Li_2CoTi_3O_8$ and $Li_2ZnTi_3O_8$ are anticipated to be good anode materials for Li ion batteries, with a high specific capacity and good cycling stability.[11,12] Hong *et al.* recently proposed $Zn_2Ti_3O_8$ as a new anode material for LIBs with excellent cycling stability and large capacity.[13] These results reveal that titanium based complex oxides are promising anode materials because of their outstanding cycling stability and high rate capability. Jiang *et al.* have analyzed the core–shell structure of CoO–$CoTiO_3$ integrated hybrid nanotube arrays (NTs) which have a capacity of 237 mA h g^{-1} at 4 A g^{-1} which is high compared to bare CoO nanowires (210 mA h g^{-1} at 4 A g^{-1}). The outer $CoTiO_3$ shell contributes less capacity, but

[a]*Solid State Ionics and Energy Devices Laboratory, Department of Physics, Bharathiar University, Coimbatore 641 046, Tamil Nadu, India. E-mail: selvankram@buc.edu.in*
[b]*Faculty of Applied Chemical Engineering, Chonnam National University, Gwangju 500-757, Republic of Korea*
[c]*Semiconductor Electronics Department, Lviv Polytechnic National University, 12 Bandera Street, Lviv 79013, Ukraine*

accommodates the volume change and preserves the morphology of the core-CoO particles during lithium insertion/deinsertion.[14]

In the present study, a new electrode of Co_2TiO_4 for Li-ion batteries is proposed. The Co_2TiO_4 has an inverse spinel ($(Co^{2+})[Co^{2+}Ti^{4+}]O_4$) structure, in which Co^{2+} ions occupy tetrahedral sites and one half of the octahedral sites, whereas the other half of the octahedral sites are occupied by Ti^{4+} ions.[15–17] Here, Co_2TiO_4 particles are prepared using a polymeric precursor method and the uniform core–shell structure of Co_2TiO_4@C is obtained through an *ex situ* hydrothermal method. The polymeric precursor method is one of the simplest ways to produce Co_2TiO_4 particles. The main advantages of the polymeric precursor method are the low cost, good chemical homogeneity at the molecular level, well controlled stoichiometry, high crystallinity and phase purity at low temperatures.[20,21] On the other hand, other wet chemical methods such as co-precipitation and hydrothermal methods lead to the formation of biphasic solid solutions and non-stoichiometric compounds.[18,19] Electrochemical studies elucidate that Co_2TiO_4@C shows a high specific capacity of 205 mA h g^{-1} at 50 mA g^{-1} over 50 cycles and when the current density was increased to 200 mA h g^{-1} it still delivers a reversible capacity of 132 mA h g^{-1} with a capacity retention of 64%. The superior cycling stability and rate capability are achieved through the intercalation behaviour of Co_2TiO_4 and the enhancement of electronic conductivity by means of the carbon shell.

2. Experimental methods

Preparation of spinel Co_2TiO_4 particles

Spinel-Co_2TiO_4 is prepared using a polymeric precursor method using citric acid as a chelating agent, while ethylene glycol acts as a polyesterification agent. Stoichiometric values of cobalt nitrate and titanium isopropoxide are used as the starting materials. Firstly, titanium isopropoxide is dissolved in aqueous citric acid solution and converted into a titanium citrate solution. The molar ratio of metal cations to citric acid was kept at 1 : 3.[22,23] Subsequently, the cobalt nitrate solution is added to the titanium citrate solution under magnetic stirring and stirred continuously for 1 h to attain a homogeneous solution. The ethylene glycol is added to the solution in a 60 : 40 weight ratio (ethylene glycol/citric acid). The above mixture is kept at 80 °C to induce the citrate polymerization process, which produces a transparent polymeric resin with slow evaporation of the water molecules. Finally, an exothermic reaction takes place when the polymeric resin was preheated at 300 °C for 1 h under an air atmosphere. The preheated sample was ground well and further calcined at different temperatures to attain phase pure Co_2TiO_4.

Preparation of spinel Co_2TiO_4@C particles

A simple and facile hydrothermal method was used to obtain a uniform core–shell structure of carbon coated Co_2TiO_4. Initially, 0.4 g of Co_2TiO_4 particles are dispersed in 40 mL of distilled water and ultrasonicated for 20 minutes. 0.8 g of glucose is added to the above solution and the process is continued for a further 30 min. The final solution was transferred into a 75 mL Teflon-lined stainless steel autoclave, sealed and maintained at 180 °C for 12 h. The hydrothermal set-up was naturally cooled down to room temperature and the obtained solid product was washed several times with distilled water and ethanol to remove the organic products and remaining ion residue. The sample was dried at 80 °C for 12 h under an air atmosphere. Finally, carbonization was carried out at 500 °C under an argon atmosphere.

Structural characterization and electrochemical measurements

X-ray diffraction analysis was carried out using a D2 PHASER desktop diffractometer with a Cu-K_α (1.54186 Å) radiation source with a step size of 0.02°. TGA analysis was carried out using a Pyris 1 TGA model instrument with a temperature range from 30 °C to 900 °C at a heating rate of 5 °C min^{-1} and nitrogen gas flow rate at 20.0 mL min^{-1}. Raman analysis was performed for the carbon coated sample using a Renishaw invia Raman microscope instrument using a He–Ne laser (633 nm) as the excitation source in the frequency range of 100–3300 cm^{-1}. XPS analysis was carried out to analyze the oxidation state of our samples using an XPS, Krato Analytical, Ultra axis instrument. The morphological features were analyzed using a JEOL JEM 2100 high resolution transmission electron microscope (HRTEM).

Electrochemical characterizations of the synthesized samples were performed using a CR2032 coin cell. The working electrodes were prepared with active material, Ketzen Black (KB) as a conductive additive and Teflonized acetylene black (TAB) as a binder in the ratio of 75 : 15 : 10 (wt%) using ethanol as the solvent. The resultant electrode film was pressed over a stainless steel current collector, followed by drying at 160 °C for 4 h before being used in the cell. The average loading of the cells was maintained at ~5 mg cm^{-2}. The cell consists of the active material as the working electrode and a metallic lithium foil as the counter electrode, separated by a polypropylene separator with 1 M $LiPF_6$ dissolved in ethylene carbonate/dimethyl carbonate (EC : DMC) 1 : 1 (v/v) as the electrolyte. Cyclic voltammetry (CV) and electrochemical impedance spectroscopy (EIS) studies were carried out using an electrochemical work station (SP-150, Biologic, France) at room temperature. The EIS spectra were measured in the frequency range between 100 kHz and 100 mHz using an applied current amplitude of 100 μA, while the CV was tested at a scan rate of 0.1 mV s^{-1} between the operating voltages of 0 V and 3.0 V *vs.* Li/Li^+. A galvanostatic charge/discharge test was carried out with a battery tester (WBCS 3000, Won-A-Tech, Korea) in the voltage range of 0–3 V under different current densities ranging from 50 mA g^{-1} to 500 mA g^{-1}. For the *ex situ* XRD analysis, multiple identical cells were made and discharged/charged to different voltages and maintained at that voltage for 3 h. They were then dismantled in a glove box, the composite electrode containing Co_2TiO_4@C was recovered and washed thoroughly with the solvent DEC to remove the electrolyte. Then, they were dried at 80 °C in a vacuum oven. For the *ex situ* XRD, the electrodes were mounted along with Cu foil.

3. Results and discussion

The phase formation of Co_2TiO_4 was analyzed using the X-ray diffraction technique (XRD). Fig. 1 shows the XRD patterns of the as prepared Co_2TiO_4 (a) and the samples calcinated for 5 h at 600 °C (b), 700 °C (c), 800 °C (d) and 900 °C (e). XRD examination revealed that the as-prepared sample shows a multi-phase composition consisting of Co_3O_4, $CoTiO_3$ and Co_2TiO_4 phases (JCPDS cards no. 78-1970, 77-1373 and 39-1410, respectively). The samples calcinated at 600 °C and 700 °C show similar phase compositions (Fig. 1(b) and (c)). The increase in the relative intensities of the peaks of $CoTiO_3$ and Co_3O_4 phases could be explained by improving the crystallinity of both these phases as a consequence of the calcination for 5 h. Increasing the calcination temperature up to 800 °C led to a remarkable improvement of the phase composition of the Co_2TiO_4 sample (Fig. 1(d)). The reflections of parasitic $CoTiO_3$ and Co_3O_4 phases disappear completely, thus only traces of $CoTiO_3$ impurities could be detected in the pattern. Further increasing the temperature to 900 °C allows us to obtain a single phase Co_2TiO_4 specimen with a cubic spinel structure (Fig. 1(e)). All observed diffraction maxima correspond to the JCPDS standard data for Co_2TiO_4 (file no. 39-1410). Corresponding *hkl* indices are depicted in Fig. 1(e).

Full-profile Rietveld refinement entirely confirms the phase purity and cubic spinel structure of the Co_2TiO_4 sample. The refinement procedure was performed in space group *Fd*3*m* based on the structural model, in which the Co^{2+} ions occupy tetrahedral 8(a) and half of the octahedral 16(d) sites, whereas the other half of the octahedral sites are occupied with Ti^{4+} species. Oxygen species are located in the general 32(e) sites (Fig. 2c). Refinement of the lattice parameters and oxygen coordinates, together with isotropic displacement parameters of all atoms shows an excellent fit between the experimental and calculated profiles (Fig. 2(a)) and led to the final atomic parameters and residuals presented in Table 1.

Refinement of the site occupancy of the octahedral and tetrahedral sites did not reveal detectable deviations from the nominal Co_2TiO_4 composition. However, the refined value of the lattice parameter $a = 8.4190(9)$ Å is somewhat smaller than the literature data for Co_2TiO_4 ($a = 8.4348$ Å, JCPDS file 39-1410). A possible reason for this may be due to the formation of a $Co_{2+x}Ti_{1-x}O_4$ solid solution with a small Co excess. According

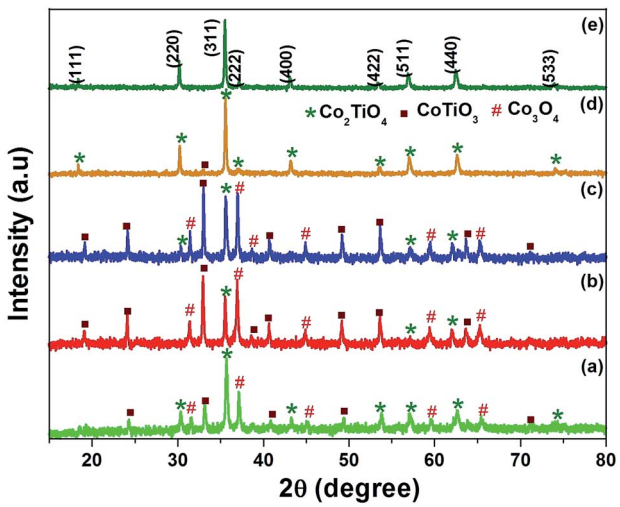

Fig. 1 XRD patterns of (a) as-prepared and (b–e) calcinated Co_2TiO_4 at different temperatures, 600 °C, 700 °C, 800 °C and 900 °C for 5 h, respectively.

Table 1 Crystallographic data for Co_2TiO_4 (S.G. *Fd*3*m*, $R_I = 0.055$, $R_p = 0.131$)

Lattice parameter	Atoms, sites	*X*	*Y*	*Z*	B_{iso}/eq., Å^2
$a = 8.4190(9)$ Å	Co1, 8a	1/8	1/8	1/8	0.7(2)
	Co2[a], 16d	1/2	1/2	1/2	0.9(2)
	O, 32e	0.2578(8)	*x*	*x*	2.4(4)

[a] Occupation: $Co2 = 0.5(2)Co^{2+} + 0.5(2)Ti^{4+}$.

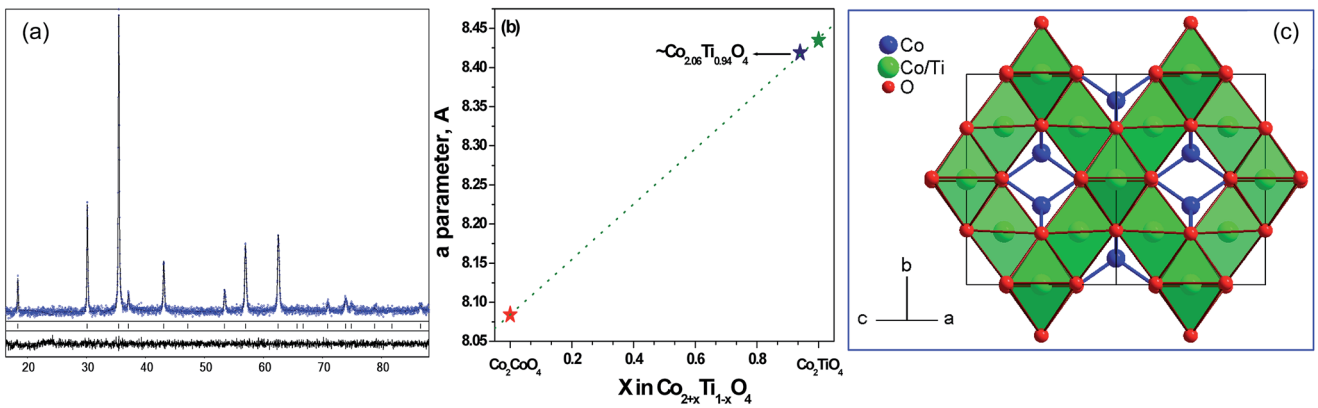

Fig. 2 (a) Graphical results of the Rietveld refinement of the Co_2TiO_4 structure. The experimental XRD pattern (blue circles) is shown in comparison with the calculated pattern. The difference between the measured and calculated profiles is shown as a curve below the diagram. The short vertical bars indicate the positions of diffraction maxima. (b) Compositional dependence of the lattice parameter in the Co_2CoO_4–Co_2TiO_4 system and (c) view of the Co_2TiO_4 inverse spinel structure as a packing of Co/TiO_6 octahedra and CoO_4 tetrahedra.

to Yankin et al,[24] the boundary of $Co_{2+x}Ti_{1-x}O_4$ solid solution is enriched in cobalt with decreasing temperatures. It should also be noted that the unit-cell parameters of Co_2TiO_4 could depend on the sintering conditions, such as temperature and oxygen pressure,[17,25] and can be caused by oxygen nonstoichiometry. From the comparison of the lattice parameter obtained for the Co_2TiO_4 sample with the literature data of Co_2TiO_4 and Co_3O_4 (Co_2CoO_4) phases, the composition of the solid solution is estimated to be $Co_{2.05}Ti_{0.95}O_4$ (Fig. 2(b)).

Fig. 3(a) shows the XRD pattern of the carbon coated Co_2TiO_4 particles, in which all the diffraction peaks coincide well with the cubic crystal structure of spinel Co_2TiO_4 (JCPDS card no. 39-1410) phase without impurity phases. The broad diffraction peaks appearing at 22° to 25° correspond to the (002) plane of low crystalline amorphous carbon which was confirmed from standard JCPDS card no. 89-8487. In order to find the weight ratio of the outer carbon shell TGA was carried out in the temperature range of 30 to 900 °C in an air atmosphere (Fig. 3b). The steep loss around 420 to 580 °C is due to the decomposition of outer shell carbon into carbon dioxide by reacting with oxygen. This confirms the composition of the inner core active material to be 83% and the outer carbon shell having 17 wt%.

The presence of the carbon coating on Co_2TiO_4 is further confirmed by Raman spectroscopy. Co_2TiO_4 has an inverse spinel structure with an O_h^7 ($Fd3m$) space group, which consists of 56 atoms ($Z = 8$) in the unit cell while the small Bravais lattice has only 14 atoms ($Z = 2$). All of these give three acoustic and 39 optical modes (42 vibrational modes). According to group theory analysis, it represents an irreducible representation of phonon modes at the Brillouin zone centre,[26]

$$\Gamma = A_{1g}(R) + E_g(R) + T_{1g} + 3T_{2g}(R) + 2A_{2u} + 2E_u + 5T_{1u}(IR) + 2T_{2u}$$

Generally, an inverse spinel structure exhibits five Raman active modes ($A_{1g} + E_g + 3T_{2g}$), five infrared active modes ($5T_{1u}$) and the remaining optical modes are silent modes ($T_{1g} + 2A_{2u} + 2E_u + 2T_{2u}$). Fig. 4(a) shows the six phonon modes of Co_2TiO_4 at 216, 259, 323, 374, 517 and 681 cm^{-1}. The phonon modes at 681 and 323 cm^{-1} are assigned to the A_{1g} and T_{2g} (2) symmetries that correspond to the symmetric and asymmetric stretching of O atoms with the metal ions in the AO_4 tetrahedron, and the peak located at 216 cm^{-1} represents the T_{2g} (1) mode that relates to the translation of the BO_6 octahedron against the A cation.[26] The phonon modes at 259 and 374 cm^{-1} are assigned to the symmetries of E_g and T_{2g} (3), respectively, which correspond to the symmetric and asymmetric bending motion of oxygen in the AO_4 tetrahedron. The Raman mode at 517 cm^{-1} is associated with the order–disorder of Co and Ti ions in the octahedral and tetrahedral sites.[27] The appearance of additional Raman modes was due to the following factors: (i) lower crystal symmetry in the crystal structure, (ii) formation of a solid solution and (iii) the presence of vacancies, which are non-predictable by the group theory.[28] The observed Raman spectrum of Co_2TiO_4 agreed well with the previous reports.[29] No other peaks are observed relating to Co_3O_4, CoO and TiO_2, which elucidates the phase purity of sample. On the other hand, the Raman spectrum of Co_2TiO_4@C shows phonon modes at 682.2 and 529 cm^{-1} (Fig. 4(b)) and the wave numbers are blue shifted from the pristine sample, which may be due to the local symmetry disorder and cation disorder of the cubic spinel structure, as observed from previous reports.[30] Two new bands arise at 1361 and 1597 cm^{-1}, which correspond to the A_{1g} vibration mode of the D-band (disordered carbon) and E_{2g} vibration mode of the G-band (graphitic carbon) (inset: enlarged view). The A_{1g} vibration is related to the vibration of

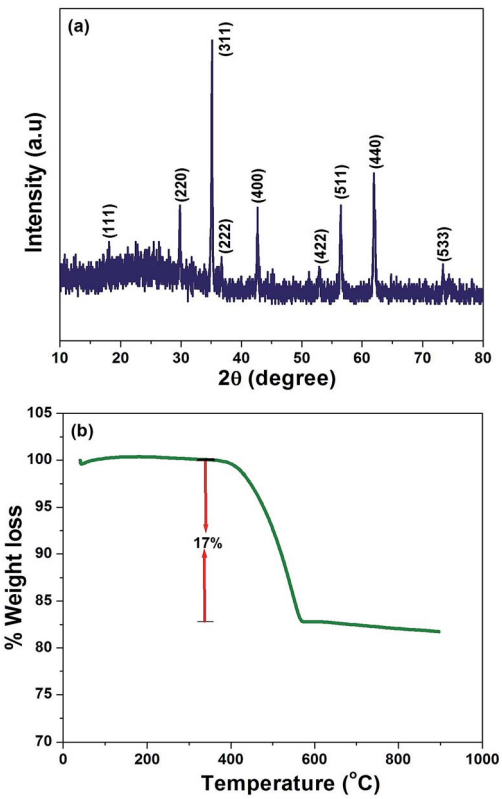

Fig. 3 (a) XRD pattern and (b) TGA curve of carbon coated Co_2TiO_4.

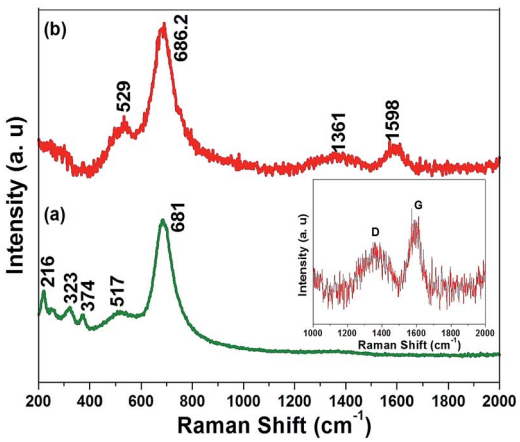

Fig. 4 Raman spectra of (a) Co_2TiO_4 and (b) carbon coated Co_2TiO_4 (inset: enlarged view).

dangling bonds in the plane edges of disordered carbon and the E_{2g} mode corresponds to the sp^2-bonded carbon atoms in a 2-dimensional graphitic layer which implies that Co_2TiO_4 particles are enfolded within a thin layer of carbon.[31,32] The D : G band ratio is one of the important factors which determines the electronic conductivity of the active material.[33] The low D : G band ratio (~0.77) assures that better electronic conductivity facilitates to enhance the electrochemical properties of the pristine material.

The species and chemical state of the elements in the carbon coated Co_2TiO_4 is analyzed using X-ray photoelectron spectroscopy. Fig. 5(a) shows the complete survey spectrum of the Co_2TiO_4@C sample with the presence of Co, Ti, O and carbon elements. The de-convoluted spectrum of cobalt is given in Fig. 5(b), which indicates the presence of two main peaks at 781.37 and 797.25 eV and two satellite peaks at 786.53 and 803.3 eV. The peaks located at 781.37 and 797.25 eV correspond to the binding energies of Co $2p_{3/2}$ and Co $2p_{1/2}$, which are associated with the Co^{2+} component. The shakeup satellite peaks at 786.53 and 803.3 eV indicate the presence of the Co^{2+} element.[34,35] In Fig. 5(c), two spin–orbit splitting is observed at 458.6 and 464.5 eV corresponding to Ti $2p_{3/2}$ and Ti $2p_{1/2}$, which indicates the presence of Ti in a +4 oxidation state.[36] Fig. 5(d) shows the de-convoluted O 1s spectrum of oxygen. The peak sitting at 530.75 eV refers to lattice oxygen sitting in the metal–oxygen (Co–O and Ti–O) framework in the crystal structure, while the peaks located at 531.91 and 533.91 eV suggest in physically adsorbed molecules (OH^- and CO^{3-}) and lattice defects due to low coordination of adsorbed molecules on the surface of the samples, respectively.[37] The de-convoluted spectrum of C 1s is shown in Fig. 5(e) which indicates the presence of functional groups in the amorphous carbon. The observed high intensity peaks at 284.6, 286.15 and 288.69 eV correspond to the sp^2 hybridized carbon (C–C), carbonyl groups and carboxylate (O–C=O) functional groups in the carbon.[38]

The morphology of the pristine and carbon coated sample was characterized by FE-SEM and HRTEM analysis. Fig. 6(a) and (b) show the FESEM and HRTEM images of Co_2TiO_4 particles which show the non-uniform shape of the micrometer sized particles with their sizes distributed in the range of 400 to 750 nm. Fig. 6(c) shows the HRTEM image of Co_2TiO_4@C particles which clearly confirms the homogeneous presence of amorphous carbon around the particles and the thickness of the carbon coating is approximately 10 nm.

The electrochemical properties of the material were studied using various techniques including cyclic voltammetry (CV), charge discharge (CD) analysis and electrochemical impedance spectroscopy (EIS). Fig. 7(a) and (b) show the galvanostatic charge–discharge curve of the pristine and carbon coated Co_2TiO_4 samples at a constant current density of 50 mA g^{-1}. In the first cycle, the discharge curve shows two regions, a plateau followed by a sloping region. The plateau region appearing at 0.80 V *vs.* Li/Li^+ corresponds to the reduction of organic electrolyte and the sloping region is attributed to the phase transition of the active material during the lithiation process. The initial discharge capacity of 1204 mA h g^{-1} was obtained due to

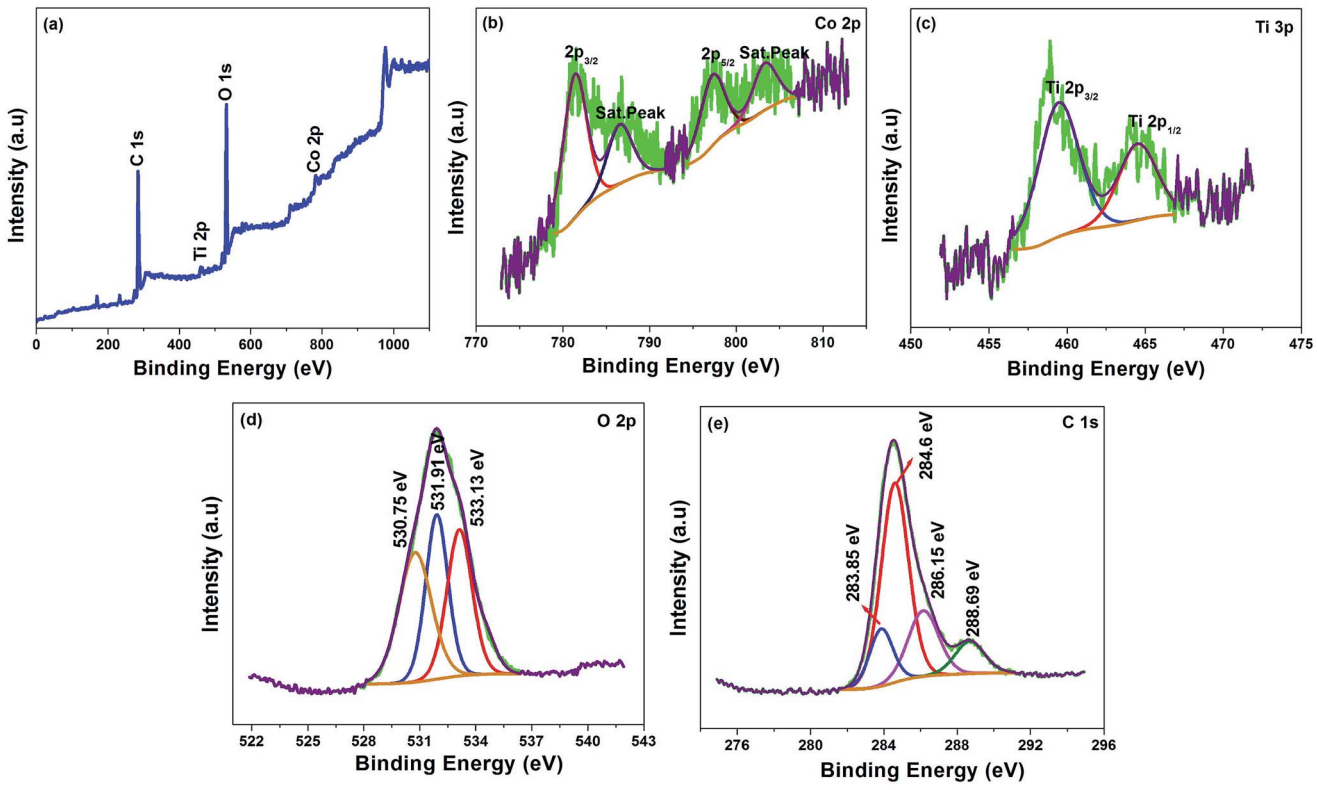

Fig. 5 (a–e) XPS survey spectrum, Co 2p, Ti 3p, O 2p and C 1s regions of Co_2TiO_4@C.

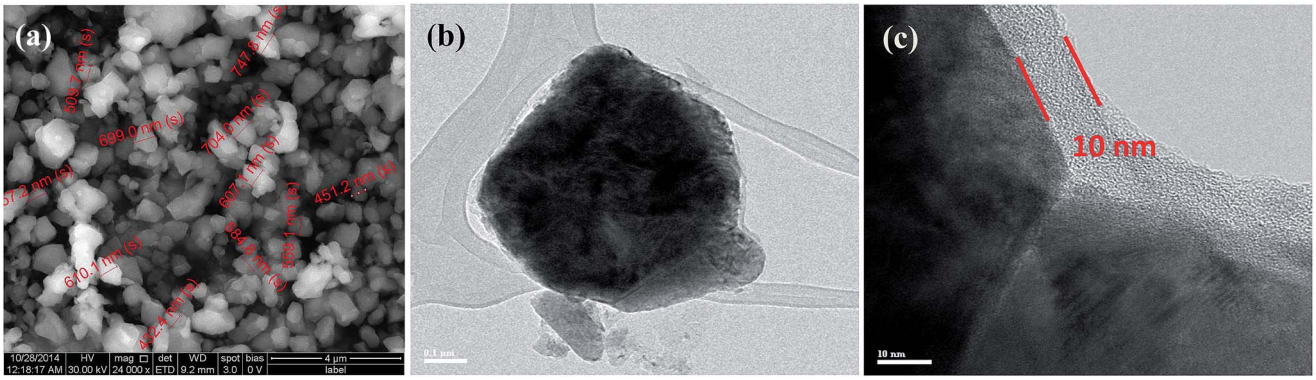

Fig. 6 (a) FESEM image of Co_2TiO_4 and (b and c) HRTEM images of Co_2TiO_4@C.

the insertion of 10 mole of lithium ions into the active material.[39,40] The observed 1st discharge–charge capacities are 1204/403 mA h g^{-1} for Co_2TiO_4 and 1283/418 mA h g^{-1} for Co_2TiO_4@C with coulombic efficiencies of 33.47 and 32.57%, respectively. The high irreversible capacity loss and low coulombic efficiency in the first cycle is attributed to the reduction of electrolyte and the formation of a SEI film.[41] In the 10th cycle, feeble capacity fading is observed due to the unstable formation of a solid electrolyte inter-phase film, and their coulombic efficiency is linearly increased to 99 and 97% for Co_2TiO_4 and Co_2TiO_4@C, respectively. After 10 cycles, they show stable discharge capacities of 138 and 205 mA h g^{-1}, which elucidates the insertion of 1.14 and 1.73 mole of Li^+ ions in the pristine and carbon coated Co_2TiO_4 over 50 cycles. This observation implies that the core–shell structure of Co_2TiO_4@C exhibits an excellent electrochemical performance compared to the pristine sample.

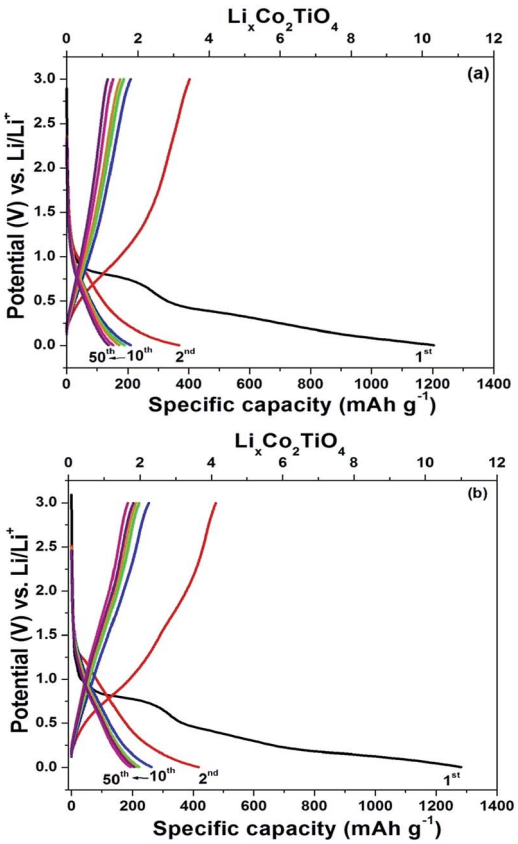

Fig. 7 (a and b) Charge–discharge curves of Co_2TiO_4 and Co_2TiO_4@C.

The cycling stability of pristine and carbon coated Co_2TiO_4 at a current density of 50 mA g^{-1} is shown in Fig. 8(a). It shows a high irreversible discharge capacity at the initial cycles followed by a few cycles of feeble capacity fading. A stabilized capacity of 137 and 205 mA h g^{-1} for Co_2TiO_4 and Co_2TiO_4@C over 50 cycles was observed with capacity retentions of 37.39% and 49.12% respectively. High capacity retention and good reversibility are attained through the uniform encapsulation of amorphous carbon on the Co_2TiO_4 particles which increase the electronic conductivity and transfer of lithium ions. And also it deliberately shows a high specific capacity compared to recently reported lithium ion insertion anode materials.[42,43] Yan *et al.* recently reported that carbon coated $Li_4Ti_5O_{12}$ anodes deliver a stable discharge capacity of 160.7 mA h g^{-1} at a 0.1C rate after 20 cycles.[42] Yang *et al.* reported a single crystalline TiO_2 cube that shows a reversible specific capacity of 203 mA h g^{-1} at a current rate of 0.5C after 100 cycles.[43] The rate capability of Co_2TiO_4 and Co_2TiO_4@C was carried out for different current densities in the potential window of 0.01–3.0 V as shown in Fig. 8(b). As the current density linearly increased from 50, 100, 200, 300, 400 and 500 mA g^{-1}, the discharge capacity values of Co_2TiO_4 were found to decrease linearly from 235, 159, 90, 70, 57 and 48 mA h g^{-1}. Meanwhile the corresponding discharge capacities of Co_2TiO_4@C were found to be 261, 196, 132, 95, 75 and 64 mA h g^{-1}, which is better than that of the pristine material. Again, when the current density was reverted back to 50 mA h g^{-1} the pristine and carbon coated samples maintain reversible capacities of 198 and 217 mA h g^{-1}, respectively, which clearly explains the good rate capability of the Co_2TiO_4@C material. The good electrochemical performance of Co_2TiO_4@C can be explained as follows: (i) the direct contact between the pristine Co_2TiO_4 and the electrolyte during the cycling process leads to agglomeration of particles and volume change that destroys the structural integrity, which leads to poor electronic conductivity. On the other hand, the protective shield of the carbon layer around the

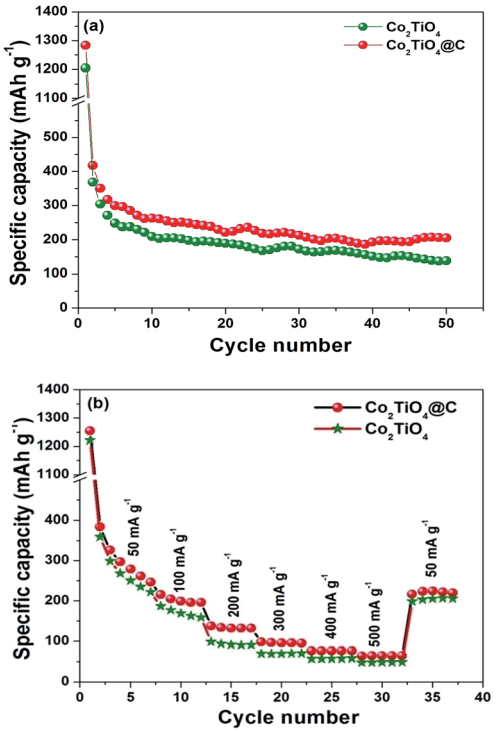

Fig. 8 (a) Cycling stability and (b) rate capability curves of Co_2TiO_4 and Co_2TiO_4@C.

Co_2TiO_4 restricts the growth of secondary agglomeration and improves the electronic conductivity between the particles. (ii) The carbon matrix also acts as a buffer layer that can accommodate the volume change and keep the structural integrity of the electrode material for long cycles. The core shell structure increases the electroactive sites thereby making more channels for electrolyte accessibility and lithium insertion/extraction minimizing the ionic resistance.[44] So all these properties collectively contribute to the enhanced electrochemical performance of the Co_2TiO_4@C particles.

The electrochemical oxidation/reduction reaction and phase transition during the charging/discharging process are identified through CV analysis in the voltage range of 3.0–0.01 V *vs.* Li/Li^+ as shown in Fig. 9(a) and (b). The Co_2TiO_4 and Co_2TiO_4@C show similar kinds of electrochemical reaction but Co_2TiO_4@C covers a high current area and well defined redox peak ascribed to a better electrochemical performance than Co_2TiO_4. In the first cycle (Fig. 9(b)), three distinct cathodic peaks are observed at 1.30, 0.58 and 0.02 V *vs.* Li/Li^+. The small reduction peak at 1.30 V is attributed to the insertion of a small amount of lithium ions into the spinel-Co_2TiO_4 crystal structure.[45] The sharp reduction peak observed at 0.58 V is attributed to the solid electrolyte interface (SEI) film formation, which is built up on the surface of the electrode material caused by electrolyte decomposition which leads to high irreversible capacity loss in the first few cycles. Co_2TiO_4 was reduced into Co, TiO_2 and Li_2O followed by a phase transition from TiO_2 to Li_xTiO_2 as described in eqn (1) and (2).[14,46] The reduction peak at 0.01 V corresponds to lithium insertion into the conducting agent and binder additives.[47] After the first cycle the cathodic/anodic peak gets stabilized at 1.55/1.65 V, 1.23/2.10 V, 0.83/1.29 V and 0.01/0.78 V as shown in Fig. 9(c). The redox pairs located at 1.55/1.65 V and 1.23/2.10 V are due to the lithium ion insertion/extraction from the TiO_2 (B) and conversion reaction (reduction/oxidation) of cobalt oxide according to eqn (3).[19,48,49] An unknown redox pair appearing at 0.83/1.29 V cannot be justified clearly because it is not related to the reduction/oxidation reaction of Ti^{4+}/Ti^{3+} and Co^{2+}/Co^{o}. However, the redox potential merely coincides with the conversion reaction of the Li_2CO_3 component as compared to earlier reports.[47,50] Li_2CO_3 mainly originates from the electrolyte decomposition of organic solvents during the discharging process, which forms the SEI layer along with inorganic species such as Li_2O, LiF and Li_2CO_3. The Li_2O and LiF formation and decomposition was electrochemically favorable for the conversion reaction of transition metal oxide anodes, but the decomposition into Li_2CO_3 is not clear yet.[51] According to Su *et al.*, the discharge process of transition metal oxides (MO_x) yields a nanosized transition metal along with the formation of Li_2O. The yielded nanosized transition metal acts as an excellent electro-catalyst, which easily reduces the Li_2CO_3 through a catalytic conversion reaction mechanism.[50] According to eqn (1), the yielded Co^0 nanoparticles facilitate the catalytic conversion reaction of the Li_2CO_3 species. In the catalytic

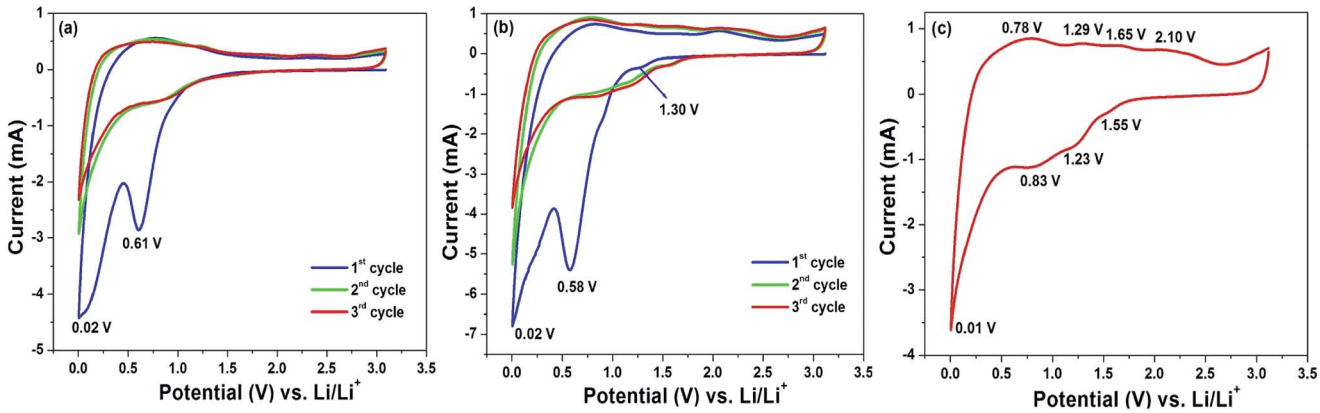

Fig. 9 (a and b) CV curves of Co_2TiO_4 and Co_2TiO_4@C, and (c) 3rd cycle of Co_2TiO_4@C.

conversion reaction, Li_2CO_3 (C^{4+}) is reduced into lower valence C^{2+} and C^0 followed by the formation of Li_2O with Li^+/electron transfer according to eqn (4) and this process causes the decomposition of the SEI layer during the cycling process.[14] The redox pair located at 0.01/0.78 V corresponds to the Li-ion insertion and extraction into/from the carbon black and binder. The electrochemical reaction mechanism has been described with the aid of CV analysis and previous reports as follows,[14,45–49]

$$Co_2TiO_4 + 4Li^+ + 4e^- \rightarrow 2Co + TiO_2 + 2Li_2O \quad (1)$$

$$TiO_2 + xLi^+ + xe^- \rightarrow Li_xTiO_2 \quad (2)$$

$$Li_xTiO_2 + 2Co + 2Li_2O \leftrightarrow 2CoO + TiO_2 + (4 + x)Li^+ + (4 + x)e^- \quad (3)$$

$$Li_2CO_3 + 5Li^+ + 5e^- \leftrightarrow 0.5Li_2C_2 + 3Li_2O \quad (4)$$

The *ex situ* XRD pattern of Co_2TiO_4 was analyzed after the first charge–discharge cycle as shown in Fig. 10. It is well known that during the first discharge reaction from the OCV to 0.01 V, the crystal structure of the starting material is destroyed followed by the reduction of metal ions into metal nanoparticles, as demonstrated in previous reports.[46] In order to confirm the above mechanism in the case of Co_2TiO_4, *ex situ* XRD was conducted on multiple cells after the initial charge and discharge process, as described in the experimental section. The XRD pattern after the initial discharge of the electrode to 0.01 V indicates the absence of Co_2TiO_4 diffraction peaks and new kinds of phases like Li_2CO_3, Li_2O, Li_2C_2, Co and Li_xTiO_2 appeared. These new phases assured that during the first discharge process, the Co_2TiO_4 crystal structure decomposed into metallic Co and Li_xTiO_2, as well as the electrolyte decomposition facilitating the formation of Li_2CO_3 and Li_2O. Again, the metallic Co acts as a catalyst which reduces the Li_2CO_3 into Li_2C_2 and Li_2O. When the electrode was charged up to 3.0 V, the Li_xTiO_2, Li_2O and Li_2C_2 peaks get subsequently suppressed. TiO_2 and CoO phases have occurred during the charging process. Thus, the *ex situ* XRD data after the charging-discharging process of the Co_2TiO_4 electrode is well supported by the CV results.[46,52]

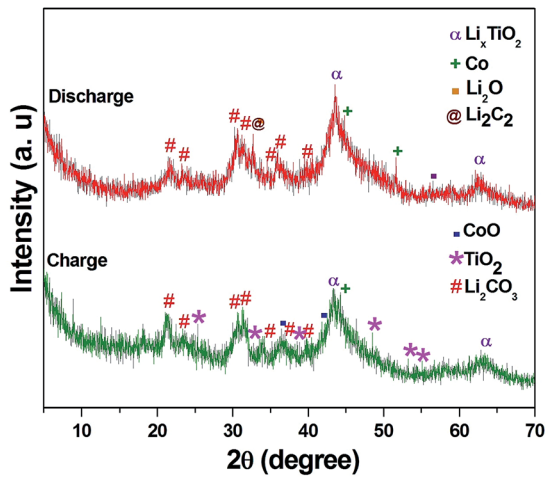

Fig. 10 The *ex situ* XRD pattern after the first discharging and charging process.

The diffusion coefficient is one of the important factors for analyzing the electrode kinetics and rate determining step during the intercalation process, which was measured through CV analysis. Fig. 11(a) and (b) show the CV curves of the pristine and carbon coated Co_2TiO_4 at different scan rates from 0.1 to 0.5 mV s^{-1}. It clearly shows that the anodic and cathodic peak currents tend to increase with increasing scan rate. The shifted anodic/cathodic peak towards low/high potential indicates that the irreversible reaction is more favourable for increasing scan rate. At a higher scan rate the lithium ions are not completely inserted/extracted into/from the electrode material due to the short time interval of the scan rate, which causes the irreversible behaviour.[53] The peak current (I_p) is directly proportional to the square root of the scan rate ($\nu^{1/2}$) (Fig. 11(c)). The curve deliberately shows a linear relationship between the peak current and scan rate suggesting a diffusion controlled process of lithium ions. The diffusion coefficient was calculated using Randles–Sevcik eqn (5),[53–55]

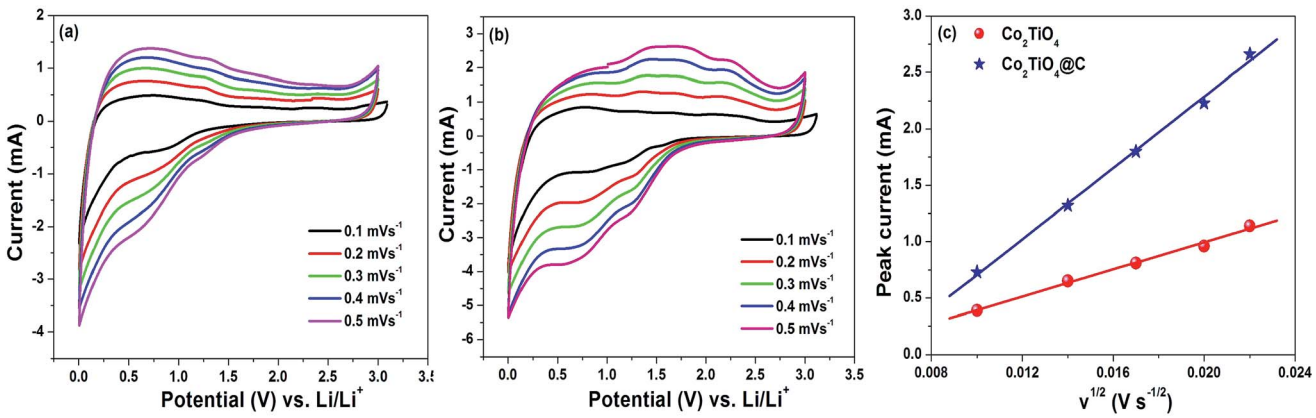

Fig. 11 (a and b) CV curves of Co_2TiO_4 and Co_2TiO_4@C at different scan rates and (c) peak current (I_p) *versus* square root of scan rate ($\nu^{1/2}$).

$$I_p = 0.4463n^{3/2}F^{3/2}C_oAR^{-1/2}T^{-1/2}D_{Li}{}^{1/2}\nu^{1/2} \quad (5)$$

where, n is the number of electrons transferred during the electrochemical reaction, F is the Faraday constant (96 486 C), C_o is the molar concentration of Li^+ ions (mol cm^{-3}), A is the area of the electrode (cm^2), R is the gas constant (8.314 J mol^{-1} K^{-1}), T is the temperature (K) and D is the diffusion coefficient (cm^2 s^{-1}). The calculated diffusion coefficient of Co_2TiO_4 is 2.55 $\times$ 10^{-11} cm^2 s^{-1} and Co_2TiO_4@C is 1.76 $\times$ 10^{-10} cm^2 s^{-1}, which elucidates that the higher diffusion coefficient of Co_2TiO_4@C is more favourable for electronic and ionic transport within the active material. This facilitates the high rate capability of the electrode material.

The role of the carbon coating on the active material and electrode kinetics was examined through electrochemical impedance spectroscopy (EIS). Fig. 12(a) and (b) show the impedance spectra of Co_2TiO_4 and Co_2TiO_4@C, before and after cycles measured in the frequency range of 100 kHz to 10 mHz at open circuit voltage. The EIS spectra is fitted with two equivalent circuits before and after cycles, it consists of solution resistance (R_S) at high frequency, solid electrolyte interface film resistance (R_{SEI}) at high to medium frequency, charge transfer resistance (R_{ct}) between the electrode/electrolyte interface at medium frequency, CPE1 and CPE2 are the constant phase elements and the slanting line at the low frequency region is known as Warburg impedance which is associated with the diffusion of lithium ions into the active material.[41,56] The EIS fitting results are shown in Table 2. It can be seen that the R_{ct} of pristine Co_2TiO_4 is 58.82 Ω and of Co_2TiO_4@C is 38.36 Ω, which elucidates that the carbon coating improves the electronic conductivity of the pristine materials. After cycling, a new semicircle appears at higher frequency which is associated with the solid electrolyte film resistance (R_{SEI}), which occurs through electrolyte decomposition that makes a passivation layer on the surface of the active material. The change in the R_{SEI} values of Co_2TiO_4 (14.64 Ω) and Co_2TiO_4@C (12.14 Ω) electrodes can be correlated with the thickness of the SEI layer since the carbon layer restricts the electrolyte decomposition on the electrodes during the cycling process, which leads to a thin SEI layer formation.[32] The R_{ct} values get reduced to 12.81 and 6.98 Ω for Co_2TiO_4 and Co_2TiO_4@C electrodes after the cycling process due to the activation process or phase change, which alter the electronic conductivity of the electrode material.[57] Still, the Co_2TiO_4@C electrode shows a low R_{ct} compared to the pristine material. Hence, the carbon layer coated on the active material enhances the electronic conductivity and lithium ion diffusion of the electrode material. The diffusion coefficient of the lithium ions was also calculated from the EIS analysis by using the following equation,[32,58]

$$D_{Li} = R^2T^2/2A^2n^4F^4C^2\sigma^2 \quad (6)$$

where, σ_w is the Warburg factor, R is the gas constant, A is the area of the electrode, F is the Faraday constant, C is the concentration of lithium ions in the electrode material and n is the number of electrons involved in the reaction. The Warburg factor (σ_w) is obtained from the slope of the linear plot between the real part of impedance (Z') and the inverse square root of the frequency (Fig. 12(c) and (d)) at low frequency regions using the following relation,[59]

$$Z' = R_S + R_{ct} + \sigma_w\omega^{-1/2} \quad (7)$$

The initial diffusion coefficient values of Co_2TiO_4 and Co_2TiO_4@C were found to be 1.38 $\times$ 10^{-13} and 6.66 $\times$ 10^{-13} cm^2 s^{-1}, whereas after cycling they were 7.95 $\times$ 10^{-13} and 1.22 $\times$ 10^{-12} cm^2 s^{-1}, respectively. The above result implies that the carbon coated Co_2TiO_4 has a higher diffusion coefficient than the pristine electrode, which supports the good rate capability of the electrode material. However, the calculated diffusion coefficient from CV and EIS analysis are deviated from each other. A similar kind of results are observed in earlier reports.[60–62] Xie *et al.* found that the diffusion coefficient

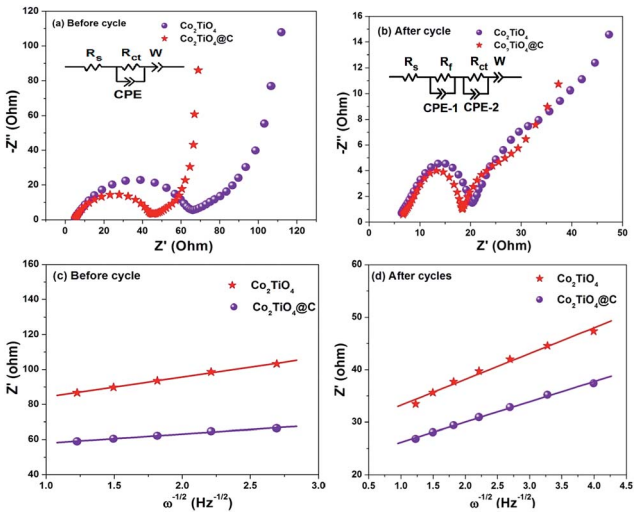

Fig. 12 (a and b) EIS spectra of before and after cycles, and (c and d) Randles plots between the real part of impedance *vs.* the inverse square root of frequency of before and after cycles, respectively.

Table 2 Electrode kinetic parameters using fitting the EIS spectra through equivalent circuit model

Sample	R_S (Ω)	R_{SEI} (Ω)	R_{ct} (Ω)	CPE1 (F)	CPE2 (F)	W (Ω)	σ_w (Ω $s^{-1/2}$)	D_{Li^+} (cm^2 s^{-1})
Co_2TiO_4 before cycle	5.13	—	58.82	54.32 $\times$ 10^{-6}	—	17.89	11.45	1.38 $\times$ 10^{-13}
Co_2TiO_4@C before cycle	5.12	—	38.36	37.40 $\times$ 10^{-6}	—	12.63	5.21	6.66 $\times$ 10^{-13}
Co_2TiO_4 after cycle	6.26	14.64	12.81	32.44 $\times$ 10^{-5}	64.42 $\times$ 10^{-3}	3.42	4.92	7.95 $\times$ 10^{-13}
Co_2TiO_4@C after cycle	6.72	12.14	6.98	38.21 $\times$ 10^{-5}	10.69 $\times$ 10^{-2}	2.56	3.85	1.22 $\times$ 10^{-12}

calculated from CV analysis was merely considered as an apparent value. EIS analysis is not providing reliable diffusion coefficient because of the following difficulties. In EIS, the diffusion coefficient is calculated from the slanting line at 45° which is related to lithium ion diffusion in the active material. But in most cases the Warburg region deviates from 45° or disappears and also it depends on the Z' and Z'' which are very sensitive to the cell construction thereby leading to unreliable diffusion coefficient values.[60] So a new kind of manipulation is needed to estimate the accurate diffusion coefficient of the electrode material.

4. Conclusions

Spinel Co_2TiO_4 particles were successfully synthesized using a polymeric precursor method. Structural analysis was carried out through Rietveld refinement which confirms the formation of spinel structure $Co_{2.05}Ti_{0.95}O_4$ particles. FE-SEM analysis shows a non uniform shape with micrometer sized particles and an HRTEM image reveals that amorphous carbon is coated on the particles with a thickness of 10 nm. CV and *ex situ* XRD analysis reveals the electrochemical oxidation/reduction reaction of Co_2TiO_4. As a negative electrodes for lithium ion batteries, Co_2TiO_4@C particles show a stable specific capacity of 205 mA h g^{-1} over 50 cycles along with enhanced rate capability. The higher diffusion coefficient value (1.76×10^{-10} cm^2 $s^{-1/2}$) of the carbon coated Co_2TiO_4, compared to the pristine material, elucidates the role of the uniform carbon shell which effectively accommodates volume strain and enhances the conductivity of the electrode material. So the above results elucidate that Co_2TiO_4@C is an efficient negative electrode material for Li-ion battery applications.

Acknowledgements

One of the authors (RKS) is grateful to UGC (No. 41-838/2012 (SR)) for their financial support under UGC-MRP. S. Yuvaraj would like to thank UGC-BSR (No. G2/5357/2013) for providing the fellowship to carry out this work successfully. L. Vasylechko acknowledges the partial support of the Ukrainian Ministry of Education and Sciences under Project "RZE".

References

1 L. Ji, Z. Lin, M. Alcoutlabi and X. Zhang, *Energy Environ. Sci.*, 2011, **4**(8), 2682–2699.
2 J. M. Tarascon and M. Armand, *Nature*, 2001, **414**, 359–367.
3 J. P. Fellner, G. J. Loeber, S. P. Vukson and C. A. Riepenhoff, *J. Power Sources*, 2003, **119–121**, 911–913.
4 Q. Zhang and X. Li, *Int. J. Electrochem. Sci.*, 2013, **8**, 6449–6456.
5 S. B. Chikkannanavar, D. M. Bernardi and L. Liu, *Power Sources*, 2014, **248**, 91–100.
6 D. Liu, W. Zhu, J. Trottier, C. Gagnon, F. Barray, A. Guerfi, A. Mauger, H. Groult, C. M. Julien, J. B. Goodenough and K. Zaghib, *RSC Adv.*, 2014, **4**, 154–167.
7 K. Persson, V. A. Sethuraman, L. J. Hardwick, Y. Hinuma, Y. S. Meng, A. van der Ven, V. Srinivasan, R. Kostecki and G. Ceder, *J. Phys. Chem. Lett.*, 2010, **1**, 1176–1180.
8 S. Scharner, W. Weppner and P. Schmid-Beurmann, *J. Electrochem. Soc.*, 1999, **146**, 857–861.
9 C. Lin, G. Wang, S. Lin, J. Li and L. Lu, *Chem. Commun.*, 2015, **51**, 8970–8973.
10 J.-T. Han, Y.-H. Huang and J. B. Goodenough, *Chem. Mater.*, 2011, **23**, 2027–2029.
11 J. Wang, H. Zhao, Y. Shen, Z. Du, X. Chen and Q. Xia, *ChemPlusChem*, 2013, **78**, 1530–1535.
12 L. Wang, L. Wu, Z. Li, G. Lei, Q. xiao and P. Zhang, *Electrochim. Acta*, 2011, **56**, 5343–5346.
13 Z. Hong, M. Wei, Q. Deng, X. Ding, L. Jiang and K. Wei, *Chem. Commun.*, 2010, **46**, 740–742.
14 J. Jiang, J. Luo, J. Zhu, X. Huang, J. Liu and T. Yu, *Nanoscale*, 2013, **5**, 8105–8113.
15 S. Ogawa and S. Waki, *J. Phys. Soc. Jpn.*, 1965, **20**, 540–545.
16 W. Lei, W.-Z. Lu, X.-H. Wang, F. Liang and J. Wang, *J. Am. Ceram. Soc.*, 2011, **94**, 20–23.
17 M. Inagaki, Y. Masuda, C. Shibata and S. Naka, *J. Inorg. Nucl. Chem.*, 1974, **36**, 2623–2624.
18 I. Packia Selvam and V. Kumar, *Mater. Lett.*, 2002, **56**, 1089–1092.
19 S. Yuvaraj, K. Karthikeyan, L. Vasylechko and R. K. Selvan, *Electrochim. Acta*, 2015, **158**, 446–456.
20 L. K. C. de Souza, J. R. Zamian, G. N. da Rocha Filho, L. E. B. Soledade, I. M. G. dos Santos, A. G. Souza, T. Scheller, R. S. Angélica and C. E. F. da Costa, *Dyes Pigm.*, 2009, **81**, 187–192.
21 V. Vinothini, P. Singh and M. Balasubramanian, *Ceram. Int.*, 2006, **32**, 99–103.
22 K. P. Lopes, L. S. Cavalcante, A. Z. Simoes, J. A. Varela, E. Longo and E. R. Leite, *J. Alloys Compd.*, 2009, **468**, 327–332.
23 E. C. Paris, E. R. Leite, E. Longo and J. A. Varela, *Mater. Lett.*, 1998, **37**, 1–5.
24 A. Yankin, O. Vikhreva and V. Balakirev, *J. Phys. Chem. Solids*, 1999, **60**, 139–143.
25 V. A. M. Brabers, *Phys. Status Solidi A*, 1972, **12**, 629–636.
26 F. J. Manjon, I. Tiginyanu and V. Ursaki, *Pressure-Induced Phase Transitions in AB_2X_4 Chalcogenide Compounds*, Springer, 2014.
27 L. Li, F. Li, T. Cui, Q. Zhou and D. Xu, *Phys. Status Solidi A*, 2012, **209**, 2596–2599.
28 M. Bouchard and A. Gambardella, *J. Raman Spectrosc.*, 2010, **41**, 1477–1485.
29 F. Casadio, A. Bezur, I. Fiedler, K. Muir, T. Trad and S. Maccagnola, Pablo Picasso to Jasper Johns, *J. Raman Spectrosc.*, 2012, **43**, 1761–1771.
30 H. S. C. O'Neill, *Eur. J. Mineral.*, 1994, **6**, 603–609.
31 T. Jawhari, A. Roid and J. Casado, *Carbon*, 1995, **33**, 1561–1565.
32 S. Yuvaraj, S. Amaresh, Y. S. Lee and R. K. Selvan, *RSC Adv.*, 2014, **4**, 6407–6416.
33 J. D. Wilcox, M. M. Doeff, M. Marcinek and R. Kostecki, *J. Electrochem. Soc.*, 2007, **154**, A389–A395.

34 S. Jin, G. Yang, H. Song, H. Cui and C. Wang, *ACS Appl. Mater. Interfaces*, 2015, **7**, 24932–24943.
35 T. Takami, *Functional cobalt oxides; Functional, Properties and Applications*, Pan Stanford Publishing Pvt.Ltd., 2014.
36 Y. Chu, J. Feng, Y. Qian and S. Xiong, *RSC Adv.*, 2015, **5**, 40899–40906.
37 Y. Changzhou, Z. Longhai, Z. Siqi, C. Hui, L. Jingdong and H. Linrui, *Nanotechnology*, 2015, **26**, 145401.
38 H. Sun, X. Sun, T. Hu, M. Yu, F. Lu and J. Lian, *J. Phys. Chem. C*, 2014, **118**, 2263–2272.
39 P. Zhang, Z. P. Guo, Y. Huang, D. Jia and H. K. Liu, *J. Power Sources*, 2011, **196**, 6987–6991.
40 C. Wang, G. Shao, Z. Ma, S. Liu, W. Song and J. Song, *Electrochim. Acta*, 2014, **130**, 679–688.
41 N. Chen, Y. Yao, D. Wang, Y. Wei, X. Bie, C. Wang, G. Chen and F. Du, *ACS Appl. Mater. Interfaces*, 2014, **6**, 10661–10666.
42 B. Yan, M. Li, X. Li, Z. Bai, J. Yang, D. Xiong and D. Li, *J. Mater. Chem. A*, 2015, **3**, 11773–11781.
43 X. Yang, Y. Yang, H. Hou, Y. Zhang, L. Fang, J. Chen and X. Ji, *J. Phys. Chem. C*, 2015, **119**, 3923–3930.
44 M. Ara, V. R. Chitturi, S. O. Salley and K. Y. S. Ng, *Electrochim. Acta*, 2015, **161**, 269–278.
45 D. Bresser, E. Paillard, R. Kloepsch, S. Krueger, M. Fiedler, R. Schmitz, D. Baither, M. Winter and S. Passerini, *Adv. Energy Mater.*, 2013, **3**, 513–523.
46 X.-F. Guan, J. Zheng, M.-L. Zhao, L.-P. Li and G.-S. Li, *RSC Adv.*, 2013, **3**, 13635–13641.
47 N. Tian, C. Hua, Z. Wang and L. Chen, *J. Mater. Chem. A*, 2015, **3**, 14173–14177.
48 M. Zukalová, M. Kalbáč, L. Kavan, I. Exnar and M. Graetzel, *Chem. Mater.*, 2005, **17**, 1248–1255.
49 L. Kavan, M. Kalbáč, M. Zukalová, I. Exnar, V. Lorenzen, R. Nesper and M. Graetzel, *Chem. Mater.*, 2004, **16**, 477–485.
50 L. Su, Z. Zhou, X. Qin, Q. Tang, D. Wu and P. Shen, *Nano Energy*, 2013, **2**, 276–282.
51 R. Wang, X. Yu, J. Bai, H. Li, X. Huang, L. Chen and X. Yang, *J. Power Sources*, 2012, **218**, 113–118.
52 D. Wang, D. Choi, Z. Yang, V. V. Viswanathan, Z. Nie, C. Wang, Y. Song, J.-G. Zhang and J. Liu, *Chem. Mater.*, 2008, **20**, 3435–3442.
53 X. H. Rui, N. Ding, J. Liu, C. Li and C. H. Chen, *Electrochim. Acta*, 2010, **55**, 2384–2390.
54 Y. Shi, L. Wen, F. Li and H.-M. Cheng, *J. Power Sources*, 2011, **196**, 8610–8617.
55 X. Lu, F. Yang, X. Geng and P. Xiao, *Electrochim. Acta*, 2014, **147**, 596–602.
56 Y. Ding, G. R. Li, C. W. Xiao and X. P. Gao, *Electrochim. Acta*, 2013, **102**, 282–289.
57 W. G. Wang, X. Wang, L. Y. Tian, Y. L. Wang and S. H. Ye, *J. Mater. Chem. A*, 2014, **2**, 4316–4323.
58 S. M. Zhang, J. X. Zhang, S. J. Xu, X. J. Yuan and B. C. He, *Electrochim. Acta*, 2013, **88**, 287–293.
59 S.-L. Chou, J.-Z. Wang, H.-K. Liu and S.-X. Dou, *J. Phys. Chem. C*, 2011, **115**, 16220–16227.
60 J. Xie, N. Imanishi, T. Matsumura, A. Hirano, Y. Takeda and O. Yamamoto, *Solid State Ionics*, 2008, **179**, 362–370.
61 K. Tang, X. Yu, J. Sun, H. Li and X. Huang, *Electrochim. Acta*, 2011, **56**, 4869–4875.
62 Y. P. Huang, T. Tao, Z. Chen, W. Han, Y. Wu, C. Kuang, S. Zhou and Y. Chen, *J. Mater. Chem. A*, 2014, **2**, 18831–18837.